Dalton Transactions

ROYAL SOCIETY OF CHEMISTRY

PAPER

View Article Online
View Journal | View Issue

Cite this: *Dalton Trans.*, 2026, **55**, 4832

Developing Ni_3N/NiO heterostructure catalysts to enhance the hydrogen evolution reaction in an alkaline medium *via* a surface-dependent mechanism

Fangfang Liu,[a] Shan Ji,*[b] Yongwei Li,[a] Zhihao Fang,[a] Vladimir Linkov,[d] Yucheng Dong*[c] and Hui Wang*[c]

In the construction of sustainable energy systems, the development of efficient and stable electrocatalysts for the hydrogen evolution reaction (HER) is of crucial significance. This study adopts an *in situ* oxidation–nitridation strategy to successfully construct a Ni_3N/NiO heterostructured catalyst with a three-dimensional hierarchical structure. In this catalyst, NiO promotes the dissociation of water molecules, while Ni_3N facilitates the generation and release of hydrogen molecules. The functional differentiation between these two materials at the interface drives the hydrogen spillover effect, synergistically accelerating the reaction rates of the basic steps in the HER. Through electrochemical testing, it is found that Ni_3N/NiO/NF exhibits excellent HER performance in 1.0 M KOH solution, requiring only 58 and 98 mV overpotentials to achieve current densities of 10 and 100 mA cm^{-2}, respectively, with a low Tafel slope of 42 mV dec^{-1}. Electrochemical impedance spectroscopy (EIS) and cyclic voltammetry (CV) analyses confirm the enhanced capability of this heterostructure in hydrogen adsorption and desorption. Ultraviolet photoelectron spectroscopy (UPS) and X-ray photoelectron spectroscopy (XPS) tests reveal electron rearrangement at the interface, verifying the existence of hydrogen spillover pathways. Additionally, the superhydrophilic–superaerophobic wetting characteristics of the catalyst surface help improve the diffusion rate of reactants and the desorption efficiency of products, thereby further enhancing the overall catalytic stability.

Received 6th January 2026,
Accepted 26th February 2026

DOI: 10.1039/d6dt00031b

rsc.li/dalton

Introduction

Developing high-performance electrocatalytic materials is one of the core technologies for achieving industrial-scale hydrogen production through water electrolysis. Ideal electrocatalysts for water electrolysis should possess key characteristics, such as high intrinsic activity, good stability, and low cost. Although noble metal catalysts demonstrate excellent activity in the hydrogen evolution reaction (HER), their high cost and resource scarcity severely limit their feasibility in large-scale applications;[1–4] meanwhile, traditional powder catalysts often lead to poor interfacial contact and structural stability issues due to their reliance on binders.[5–7] Therefore, in recent years, the growth of transition metal-based catalysts on self-supporting materials has become an active research topic. Transition metal-based catalysts not only possess good mechanical strength and structural stability but also enable precise control of electrocatalytic performance through fine-tuning of their composition, morphology, and electronic structure. For example, transition metal nitrides, phosphides, and other materials exhibit high similarity to noble metal catalysts in catalytic behavior due to their unique electronic structures, especially when introducing heteroatom doping, constructing heterogeneous structures, and inducing defects, which significantly enhance their intrinsic catalytic activity.[8–13] Meanwhile, self-supporting structures help avoid the use of binders, thereby improving the electron and mass transfer efficiency and enhancing the electrochemical stability of catalysts.[14–17] Therefore, employing comprehensive strategies of material component optimization, interface structure regulation, and conductive carrier design is a feasible approach for constructing efficient and stable HER electrode materials.

The HER involves a series of sequential elementary steps, each of which is kinetically influenced by the adsorption behavior of intermediates.[18,19] Therefore, the design of efficient

[a]*Shandong Engineering Research Center of New Energy Materials and Devices, Weifang University of Science and Technology, 262700 Weifang, China*
[b]*College of Biological Chemical Science and Engineering, Jiaxing University, 314001 Jiaxing, China*
[c]*College of Chemical Engineering, Qingdao University of Science and Technology, 266042 Qingdao, China*
[d]*South African Institute for Advanced Material Chemistry, University of the Western Cape, Cape Town, 7535, South Africa*

electrocatalysts should precisely regulate each elementary step.[1,20] Previous studies have shown that the composition configuration, morphology control, and electronic structure adjustment of catalysts can significantly affect the rate control of elementary steps, such as water molecule cleavage, adsorption of hydrated hydrogen (H_{ad}), and desorption of hydrogen gas.[21–24] Based on this, constructing heterogeneous structures with interfacial synergistic effects is considered an effective strategy to enhance HER activity. For example, Zhao *et al.*[25] used Density Functional Theory (DFT) to predict the function of NiO and experimentally verified by controlling the surface component ratio of nickel/nickel oxide (Ni/NiO) nanocrystals that NiO can promote the Volmer step, while Ni is favorable for the Heyrovsky/Tafel steps. After optimization, when the nickel/nickel oxide ratio is 23.7%, the adsorption–desorption steps reach an optimal balance, resulting in the best intrinsic activity of the nickel/nickel oxide catalyst. Binary catalysts can also introduce hydrogen spillover effects through hydrogen transfer between different phases.[26,27] Research by Li *et al.*[28] shows that when the work function difference ($\Delta\Phi$) between platinum (Pt) and cobalt phosphide (CoP) is small, the proton adsorption potential at the interface is reduced, thereby promoting hydrogen transfer (spillover) between the two phases. By adjusting the $\Delta\Phi$ values between platinum and different metals (such as rhodium (Rh), palladium (Pd), *etc.*), fine tuning of HER kinetics can be achieved. Their results show that PtIr/CoP exhibits the best HER activity when $\Delta\Phi$ is minimal. The introduction of hydrogen spillover significantly accelerates the transfer rate of hydrogen atoms in the reaction, improving the overall reaction rate. Evidently, by regulating the composition and structure of catalysts, the intrinsic activity of the hydrogen evolution reaction can be enhanced.

It must be pointed out that enhancing intrinsic activity is not the only factor of concern in the industrialization process of the HER. In practical applications, catalysts still need to maintain excellent performance under high current density conditions, and at this point, the rapid transport of reactants and effective detachment of product bubbles become core issues.[29–33] Hydrophilic surfaces facilitate the diffusion and adsorption of water molecules, while gas-phobicity is beneficial for the rapid release of bubbles and re-exposure of active sites.[34–37] The super gas-philic/gas-phobic synergistic electrode (SAL/SAB) constructed by Zhang *et al.*[30] significantly improved the hydrogen diffusion efficiency by regulating the gas wettability of the electrode surface, achieving a high HER current density of 1867 mA cm^{-2} at an overpotential of only 500 mV. Therefore, designing catalytic materials with high activity and advanced surface properties can achieve synergistic enhancement of reaction kinetics and mass transport kinetics, thereby accelerating the HER reaction rate.

Based on the above research progress and challenges, this study designed and synthesized a self-supporting heterostructured catalyst composed of Ni_3N and NiO. This catalyst's structure combines the excellent performance of NiO in water dissociation with the significant advantages of Ni_3N in hydrogen adsorption. Through precise regulation of the two-phase interface, a work function difference was formed. This approach successfully induced directional hydrogen spillover pathways at its heterogeneous interface, achieving fine regulation of the synergistic catalytic effect throughout the HER process. Through detailed morphology control, comprehensive structural characterization, extensive electrochemical performance testing, and in-depth *in situ* spectroscopic analysis, this study thoroughly reveals the electronic behavior and kinetic mechanisms of the Ni_3N/NiO interface in promoting hydrogen adsorption, transfer, and desorption processes, and verifies the excellent catalytic activity and stability exhibited by this material at high current densities.

Experimental section

Pre-treatment of nickel foam

Nickel foam of size 2 × 3 cm^2 was immersed in 3 M hydrochloric acid solution and ultrasonically treated for 15 minutes to remove its surface oxide layer. The treated nickel foam was washed sequentially with ultrapure water and ethanol, followed by vacuum drying at 60 °C.

Preparation of Ni_3N/NiO/NF

The pretreated nickel foam was immersed in 20 mL of dilute hydrochloric acid solution with a concentration of 3.6 × 10^{-3} M. The solution was then transferred to a 100 mL autoclave and maintained at 100 °C for 20 hours. After that, the sample was washed with ultrapure water and vacuum-dried at 60 °C. The resulting sample was labeled as $Ni(OH)_2$/NF. The as-prepared $Ni(OH)_2$/NF was placed in a porcelain boat and inserted into a tube furnace. It was heated to 350 °C at a rate of 10 °C min^{-1} and held at this temperature for 120 minutes. The sample obtained through this process was denoted as NiO/NF. Subsequently, the prepared NiO/NF was put in a porcelain boat and again moved into the tube furnace. The furnace was first purged with N_2 for 15 minutes to completely remove air, after which NH_3 gas was introduced and maintained for 15 minutes at a flow rate of 20 mL min^{-1}. The temperature was then raised to 350 °C, 400 °C, 450 °C, and 500 °C at a heating rate of 10 °C min^{-1}, with a holding time of 60 minutes for each temperature. The final products were labelled as Ni_3N/NiO/NF-350, Ni_3N/NiO/NF, Ni_3N/NiO/NF-450, and Ni_3N/NiO/NF-500, respectively.

Physical characterization

The morphology of the as-prepared materials was thoroughly examined using a Carl Zeiss Ultra Plus field-emission scanning electron microscope (SEM). The contact angle of bubbles under the electrolyte was accurately measured *via* the captive-bubble method using a 25-gauge needle with a CAST 3.0 system, and the data were fitted using the Axisymmetric Drop Shape Analysis–Young–Laplace method. The wettability of the electrolyte was determined at 0.8 cm using the pendant drop method. X-ray diffraction (XRD) analysis was performed using a Shimadzu XD-3A instrument equipped with a source of fil-

tered Cu-Kα radiation (λ = 0.15418 nm), operating at 30 mA and 40 kV. The XRD patterns were recorded at a rate of 5° min^{-1} over the 2θ range of 30–90°. Transmission electron microscopy (TEM), high-angle annular dark-field scanning TEM (HAADF-STEM) imaging, and selected-area electron diffraction (SAED) analysis were carried out using a JEOL JEM-2000 FX microscope operating at 200 kV. X-ray photoelectron spectroscopy (XPS) analysis was performed using a VG Escalab210 spectrometer equipped with an Mg 300 W X-ray source. The nitrogen content of the samples was determined using an ONH-3000 oxygen, nitrogen, and hydrogen analyzer. The ultraviolet photoelectron spectra (UPS) of the samples were recorded with HeI irradiation of hv = 21.21 eV using a Thermo Fisher ESCALAB 250Xi spectrometer.

Electrochemical characterization

The electrochemical measurements in this study were conducted using a CHI760e electrochemical workstation using Hg/HgO as the reference electrode and a graphite rod as the counter electrode. The measured potentials were converted to the reversible hydrogen electrode (RHE) using the equation $E_{RHE} = E_{Hg/HgO} + 0.059pH + 0.098$ V. Linear sweep voltammetry (LSV) was performed at a scan rate of 5 mV s^{-1}, and all polarization curves were *iR*-compensated (95%). Electrochemical impedance spectroscopy (EIS) measurements were carried out within a frequency range from 0.01 Hz to 100 kHz. The electrochemical double-layer capacitance (C_{dl}) of the samples was determined by cyclic voltammetry (CV) within a non-faradaic potential window. The potential–time response was recorded *via* chronopotentiometry (CP) at a current density of 10 mA cm^{-2} for 10 hours.

Results and discussion

Fig. 1a illustrates the synthetic process of the self-supporting three-dimensional heterostructured Ni_3N/NiO/NF catalyst.

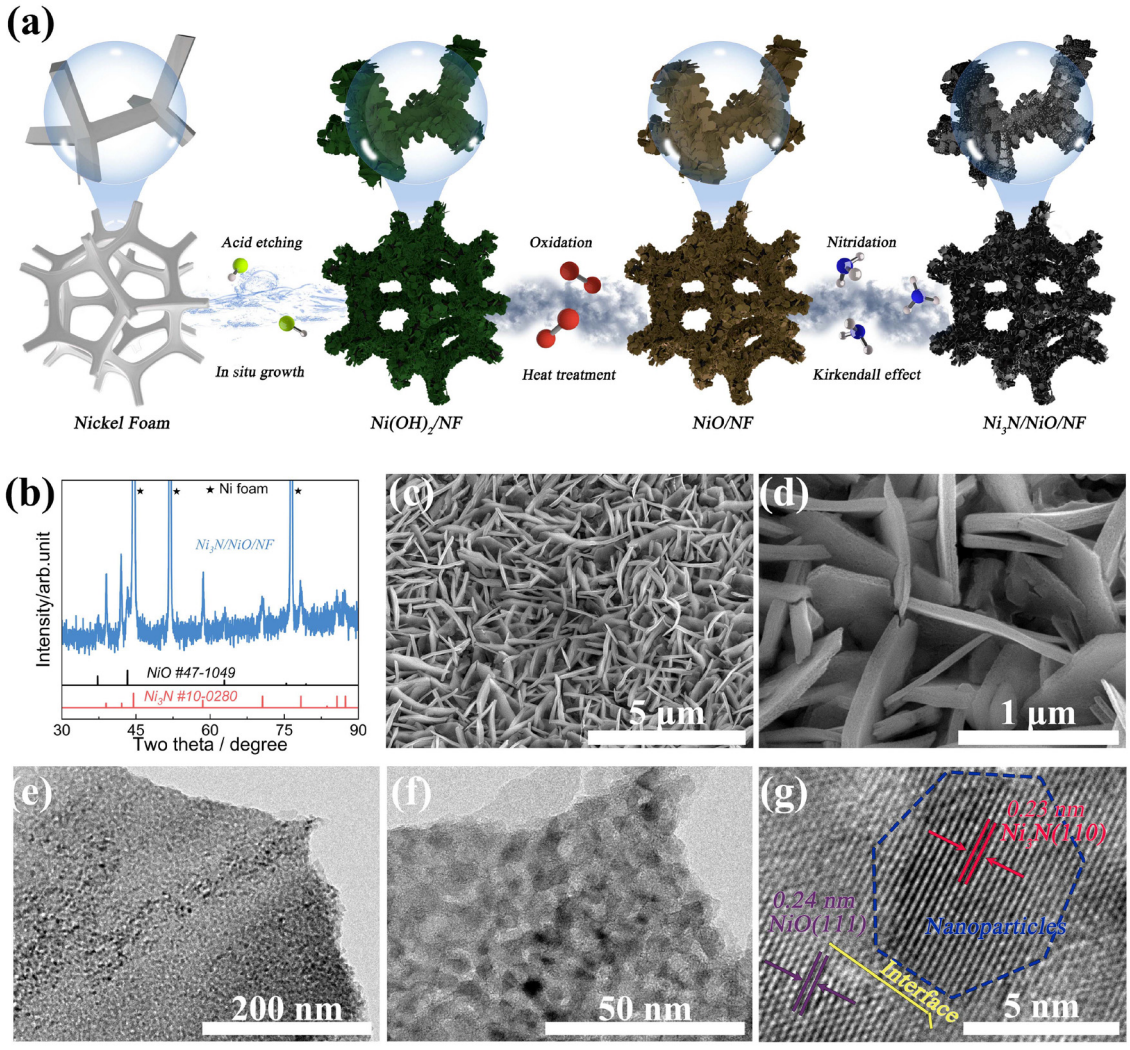

Fig. 1 (a) Schematic diagram of the synthesis process of the self-supporting heterostructured Ni_3N/NiO/NF catalyst. (b) XRD pattern of the Ni_3N/NiO/NF material. (c and d) SEM images, (e) TEM image, and (f and g) HR-TEM images of Ni_3N/NiO/NF.

Based on our works,[38] this study employed an *in situ* acid etching technique to prepare the Ni_3N/NiO/NF catalyst. By controlling the pH value during the hydrothermal reaction, the displaced Ni^{2+} ions are deposited on the smooth nickel foam substrate (Fig. S1), forming uniform and smooth $Ni(OH)_2$ nanosheet structures (Fig. S2 and S3a–c). From the SEM images of the NiO/NF sample (Fig. S3d–f), it is evident that the nanosheet structure does not undergo significant changes after oxidation treatment. This oxidation process serves a dual purpose: it preserves the nanosheet integrity during nitriding (Fig. S4 shows severe damage to the Ni_3N/NF morphology) and enhances the material's surface energy. Subsequently, annealing at 400 °C under an ammonia atmosphere aims to reduce part of the NiO to Ni_3N. The XRD pattern (Fig. 1b) clearly indicates the diffraction peaks of Ni_3N (PDF# 10-0280) and NiO (PDF# 47-1049) in addition to Ni peaks, confirming the successful synthesis of the heterostructured Ni_3N and NiO on the nickel surface. The nitriding temperature significantly affects the morphology of the product nanosheets. When the nitriding temperature is between 350 °C and 400 °C, the Kirkendall effect promotes Ostwald ripening, causing nanoparticles to aggregate on the nanosheet surface, forming an uneven nanoparticle structure. During this process, the NiO substrate separates from the Ni_3N nanoparticles, and the roughness of the nanosheets gradually increases (Fig. S5a–c and Fig. 1c and d). However, when the nitriding temperature is increased to 450 °C and then 500 °C, the erosion effect of ammonia on the nanosheets causes the structure to gradually deteriorate until it essentially disappears (Fig. S5d–i). To further investigate the changes in crystal structure during the preparation process, XRD analysis was performed. The temperature gradient shown in Fig. S6a indicates that only the Ni_3N/NiO/NF sample clearly shows the coexistence of Ni_3N and NiO. By comparing the XRD patterns of Ni_3N/NiO/NF, Ni_3N/NF, NF–N, and NiO/NF (Fig. S6b), it was found that the diffraction peak positions of Ni_3N and NiO remained almost unchanged, further confirming the separation of the NiO substrate from the Ni_3N nanoparticles.

The Transmission Electron Microscopy (TEM) technique was used to investigate the microstructural and compositional changes of catalyst materials before and after nitridation. As shown in Fig. S7a–c, the nanosheets of the NiO/NF material exhibit highly flat and smooth surfaces. In the High-Resolution Transmission Electron Microscopy (HR-TEM) images, lattice fringes corresponding to the (111) crystal plane of NiO are clearly visible. Selected Area Electron Diffraction (SAED) analysis revealed six diffraction rings pointing to NiO crystal planes (Fig. S7d), while Energy Dispersive X-ray (EDX) analysis (Fig. S7e) further confirmed the presence of O and Ni elements in the material. After nitridation treatment, Ostwald ripening was observed, with atoms agglomerating and sintering to form nanoparticles, while simultaneously creating porous structures on the nanosheet surface (Fig. 1e). At this stage, the porous structure between nanosheets and nanoparticles endowed the catalyst surface with rich interfacial characteristics, while the electrode material as a whole exhibited a three-dimensional structure (Fig. 1f). The HR-TEM image of Ni_3N/NiO/NF reveals that the size of the nanoparticles is approximately 6 nm, with internal lattice fringes of 0.23 nm corresponding to the Ni_3N(110) crystal plane. The lattice fringes with a spacing of 0.24 nm in the nanosheet region outside the nanoparticles are attributed to the NiO(111) crystal plane, with a distinct heterostructure interface between the two phases (Fig. 1g). Five concentric circles appearing in the SAED pattern correspond to different crystal planes of NiO and Ni_3N (Fig. S8a). EDX analysis further confirmed the presence of Ni, N, and O elements in the sample (Fig. S8b). Elemental mapping analysis showed that Ni and O elements are densely distributed, while N elements are distributed in a dotted pattern, which may correspond to the nanoparticles in the TEM image, *i.e.*, the Ni_3N phase. Meanwhile, the vacant areas in the elemental mapping represent the presence of porous structures (Fig. S8c–f).

To evaluate the HER activity of the synthesized binary heterostructured catalytic materials, a three-electrode system was employed in this study to conduct linear sweep voltammetry (LSV) tests in 1.0 M KOH electrolyte. As shown in Fig. 2a, compared to NF, $Ni(OH)_2$/NF, NiO/NF and Ni_3N/NF without oxidation treatment, Ni_3N/NiO/NF exhibited the highest HER activity. Additionally, as shown in Fig. S9, among the samples prepared at different temperatures, the Ni_3N/NiO/NF synthesized at 400 °C exhibited the best performance. For quantitative comparison of catalytic activity, overpotential histograms at current densities of 10 and 100 mA cm^{-2} were plotted (Fig. 2b), showing that Ni_3N/NiO/NF required overpotentials of only 58 mV and 98 mV to reach these current densities, respectively. By fitting the Tafel curves to the Faraday region of the LSV plots (Fig. 2c), the HER kinetic characteristics of these prepared samples were evaluated. Compared to NF, $Ni(OH)_2$/NF, and NiO/NF, which are controlled by the Volmer step, Ni_3N/NiO/NF and Ni_3N/NF exhibited faster kinetics associated with the Heyrovsky step, indicating that the adsorption of active hydrogen at reaction centers is not the key factor determining HER rate, whereas the hydrogen-desorption process begins to act as the bottleneck limiting the overall reaction rate. Among these samples, Ni_3N/NiO/NF showed a Tafel slope of 42 mV dec^{-1}, approaching the Tafel step. Since NiO in the binary catalyst has difficulty adsorbing the hydrogen intermediate H_{ad} (controlled by the Volmer step), this suggests that the Ni_3N/NiO/NF material with its binary heterostructure exhibits faster hydrogen-desorption capability compared to the single-phase Ni_3N/NF sample.

By recording CV curves at different scan rates (Fig. S10 and S11a), this study calculated the electrochemical double-layer capacitance values to evaluate the electrochemically active surface area (ECSA) of these samples. As shown in Fig. 2d, the double-layer capacitance (C_{dl}) values of Ni_3N/NiO/NF, Ni_3N/NF, $Ni(OH)_2$/NF, and NF were 2.13, 2.51, 1.22, and 1.00 mF cm^{-2}, respectively (NiO/NF was not included due to its redox reactions in this scan region). The C_{dl} values of samples prepared at different nitridation temperatures were generally consistent with the SEM results (Fig. S11b). Based on the calculations,

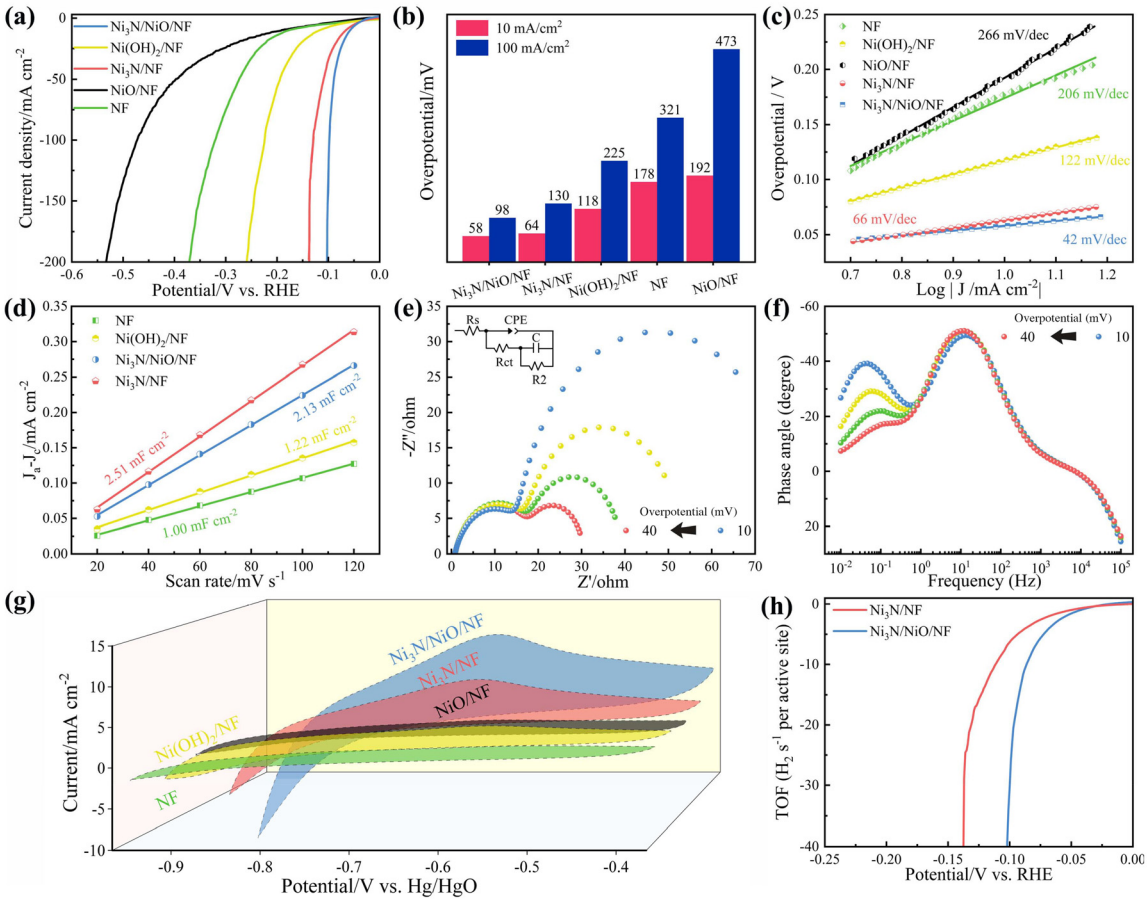

Fig. 2 (a) Linear sweep voltammetry (LSV) curves of NF, $Ni(OH)_2$/NF, NiO/NF, Ni_3N/NF, and Ni_3N/NiO/NF in 1 M KOH solution. (b) Bbar chart showing the relationship between overpotential and current density. (c) Tafel slope curves. (d) Linear fitting graph of Δj *vs.* scan rates. (e) Nyquist plot of Ni_3N/NiO/NF. (f) Bode plot. (g) Cyclic voltammetry (CV) curves of NF, $Ni(OH)_2$/NF, NiO/NF, Ni_3N/NF, and Ni_3N/NiO/NF at a scan rate of 50 mV s^{-1}. (h) Turnover frequency (TOF) curves of Ni_3N/NF and Ni_3N/NiO/NF.

the ECSA values are shown in Table S1, with the Ni_3N/NiO/NF and Ni_3N/NF materials exhibiting similar ECSA values. Further calculation of the specific activity per area as shown in Fig. S12 reveals that Ni_3N/NiO/NF still demonstrates high activity in the HER, thus excluding the potential influence of the ECSA on HER activity performance.

If Ni_3N/NiO/NF is assumed to exhibit synergistic catalytic effects, its hydrogen adsorption and desorption characteristics would differ significantly from those of other catalytic materials. The aforementioned hypothesis can be verified by *in situ* monitoring of hydrogen adsorption and desorption behavior of the catalyst. An in-depth investigation of the hydrogen adsorption characteristics of the catalytic material was first conducted in this study. Electrochemical impedance spectroscopy (EIS), as an effective means to understand electrochemical reaction kinetics, is particularly suitable for studying the adsorption and desorption kinetics of reactants on electrode surfaces.[39,40] Fig. 2e shows the Nyquist plots of Ni_3N/NiO/NF in the range of 10–40 mV, and the corresponding Bode plots reveal two time constants (Fig. 2f), each corresponding to a physical phenomenon or reaction process.[41,42] The characteristics of the two relaxation processes are located at frequencies of 10^{-1} Hz and 10^{1} Hz, respectively, simulated using a dual time constant parallel model. This model consists of a series resistance R_s and a dual parallel branch, where R_s in the high-frequency region represents the basic solution resistance. The first parallel component (CPE–R_{ct}) in the parallel branch reflects the charge transfer process of the catalyst in the mid-frequency region, while the second parallel component (C_φ and R_2) reveals the hydrogen adsorption behavior on the catalyst surface in the low-frequency region.[43–45] As shown in Fig. S13 and 14, other catalysts did not show significant hydrogen adsorption-related responses, indicating that hydrogen adsorption had reached saturation at very low potentials (when lacking responses related to hydrogen adsorption, the catalysts were simulated using single time constant models and dual time constant series models, respectively). The fitted parameters are shown in Tables S2–S4. At the same potential, all catalysts have similar R_s values, indicating that the test conditions are basically consistent. Additionally, the charge transfer resistance R_{ct} values of different catalysts correspond to their HER performances, with the smallest R_{ct} value indicating

that Ni_3N/NiO/NF has a highly conductive network, thereby providing fast charge transfer kinetics for the HER. On the other hand, the integral of C_φ and η can quantitatively describe the hydrogen adsorption charge (Q_H) on the catalyst surface. Compared with catalysts such as Ni_3N/NiO/NF, NiO/NF, NF, Ni$(OH)_2$/NF, Ni_3N/NiO/NF-350, Ni_3N/NiO/NF-450, and Ni_3N/NiO/NF-500, the Ni_3N/NiO/NF catalyst with its obvious hydrogen adsorption response clearly exhibits an abnormally high amount of hydrogen adsorption, which may be due to the re-exposure of adsorption sites caused by the hydrogen spillover effect, significantly increasing the amount of hydrogen adsorption on the catalyst surface. Notably, at different potentials, the first parallel component of Ni_3N/NiO/NF remains basically unchanged, while the second parallel component gradually decreases as hydrogen adsorption gradually reaches saturation.

Furthermore, the hydrogen desorption characteristics of the prepared catalysts were investigated by cyclic voltammetry (CV). As shown in Fig. 2g, the peak observed in the potential range of −0.7 to −0.6 V (*vs.* Hg/HgO) can be attributed to the hydrogen desorption peak.[46,47] For the NiO/NF, Ni$(OH)_2$/NF, and NF samples, the intensity of the hydrogen desorption peak is extremely weak, consistent with their poor Tafel kinetics, indicating their limited hydrogen adsorption/desorption capacity. In contrast, the Ni_3N/NF and Ni_3N/NiO/NF samples exhibit pronounced hydrogen desorption peaks. When comparing the two, the Ni_3N/NiO/NF sample exhibits a significantly higher hydrogen desorption peak intensity. Integration analysis of the desorption peak region reveals that the integrated areas for Ni_3N/NiO/NF and Ni_3N/NF are 1.97 and 1.14, respectively. The nearly doubled hydrogen desorption capacity of the Ni_3N/NiO/NF catalyst provides clear evidence that excess adsorbed hydrogen atoms (H_{ad}) on the active Ni_3N sites are diverted to another pathway—spillover to the NiO phase. This phenomenon indicates the occurrence of a hydrogen spillover effect in the Ni_3N/NiO/NF material.

To gain better insight into the intrinsic reaction performance of the catalytically active sites, oxygen–nitrogen–hydrogen (ONH) analysis was performed on these catalysts (Table S5), and their turnover frequency (TOF) was calculated to characterize the number of H_2 molecules generated per active site per second. This further eliminated the potential influence of the number of active sites on HER activity. As shown in Fig. 2h, at an overpotential of 53 mV, the TOF value of Ni_3N/NiO/NF reached 2.36 s^{-1}, compared to 1.84 s^{-1} for Ni_3N/NF. Although the number of active sites in Ni_3N/NiO/NF was approximately 30% lower than that in Ni_3N/NF, its turnover frequency increased by 30%. This result strongly demonstrates the higher hydrogen conversion efficiency of Ni_3N in Ni_3N/NiO/NF. A comparison of Fig. S15 and Table S6 shows the performance and Tafel slopes of various electrode materials, demonstrating that the Ni_3N/NiO/NF electrode outperforms or is in a superior position compared to the electrodes reported in other published studies.

Surface charge distribution plays a critical role in catalytic processes, particularly in binary heterostructures where charge transfer mechanisms at interfacial regions significantly influence catalytic activity. According to solid-state band theory, electron transfer phenomena are closely related to the work function of materials. At heterointerfaces with distinct Fermi level differences, Schottky heterostructures readily form, facilitating the migration of active H_{ad} from hydrogen-rich to hydrogen-deficient regions, thereby inducing hydrogen spillover. To validate the possibility of hydrogen spillover, ultraviolet photoelectron spectroscopy (UPS) was performed on the relevant materials, and the individual ionization energy values, equivalent to the work function (Φ) in metallic materials, were compared.[48,49] As shown in Fig. 3a and b, the work functions of Ni_3N/NF and NiO/NF were estimated to be 7.01 eV and 7.61 eV, respectively, satisfying the conditions for forming a Schottky barrier band structure. As shown in Fig. 3c, upon contact between the heterogeneous components, the energy bands of the NiO phase bend downward, and electrons redistribute at the interface until the Fermi levels of the two components equilibrate.[50,51] Specifically, in the Ni_3N/NiO/NF system, self-driven electron transfer at the heterointerface leads to an increased Ni valence state on the Ni_3N side and a decreased Ni valence state on the NiO side. Consequently, a local nucleophilic region forms in the NiO domain, while a local electrophilic region forms on the Ni_3N side.

X-ray photoelectron spectroscopy (XPS) was subsequently used to verify the valence state changes caused by charge reorganization. Specifically, a comparative analysis of high-resolution Ni $2p_{3/2}$, N 1s, and O 1s XPS spectra was performed on three catalysts: Ni_3N/NiO/NF, Ni_3N/NF, and NiO/NF. The XRD analysis results were consistent with the XPS full spectrum analysis, both confirming the presence of Ni, O, and N elements in Ni_3N/NF and Ni_3N/NiO/NF, while the NiO/NF sample contained only Ni and O elements (Fig. S16 and 17). The electron transfer phenomenon between binary components was further explored using high-resolution Ni $2p_{3/2}$ spectra. The Ni $2p_{3/2}$ spectrum of Ni_3N/NiO/NF exhibited three spin–orbit peaks and one satellite peak, mainly composed of Ni^{2+} (855.31 eV), Ni^{1+} (853.76 eV), and Ni^0 (852.85 eV) (Fig. 3d).[52,53] Notably, due to the imbalance of Fermi levels between the Ni_3N and NiO phases, self-driven electron transfer occurred from the Ni_3N phase to the NiO phase. Compared with Ni^{1+} (853.37 eV) and Ni^0 (852.40 eV) in the Ni_3N/NF sample, Ni^{1+} and Ni^0 in Ni_3N/NiO/NF shifted toward higher binding energies by 0.39 eV and 0.45 eV, respectively. Compared to the Ni^{2+} peak (855.38 eV) in the NiO/NF sample, the Ni^{2+} peak in the Ni_3N/NiO/NF sample shifts by 0.08 eV toward lower binding energy. Similarly, as shown in Fig. 3e, the high-resolution N 1s spectra of the Ni_3N/NiO/NF and Ni_3N/NF samples could be fitted into three peaks: 397.57 eV, 398.03 eV, and 398.49 eV, corresponding to N–M, N–O, and N–H, respectively.[54–56] Compared with N–M (397.57 eV) in the Ni_3N/NF sample, N–M (398.03 eV) in the Ni_3N/NiO/NF sample shifted toward higher binding energy by 0.46 eV, consistent with the trend of changes in Ni^{1+} and Ni^0. In the O 1s spectrum (Fig. 3f), the peaks of the Ni_3N/NiO/NF and NiO/NF samples corresponded to M–O (O_I), O-containing groups (O_{II}),

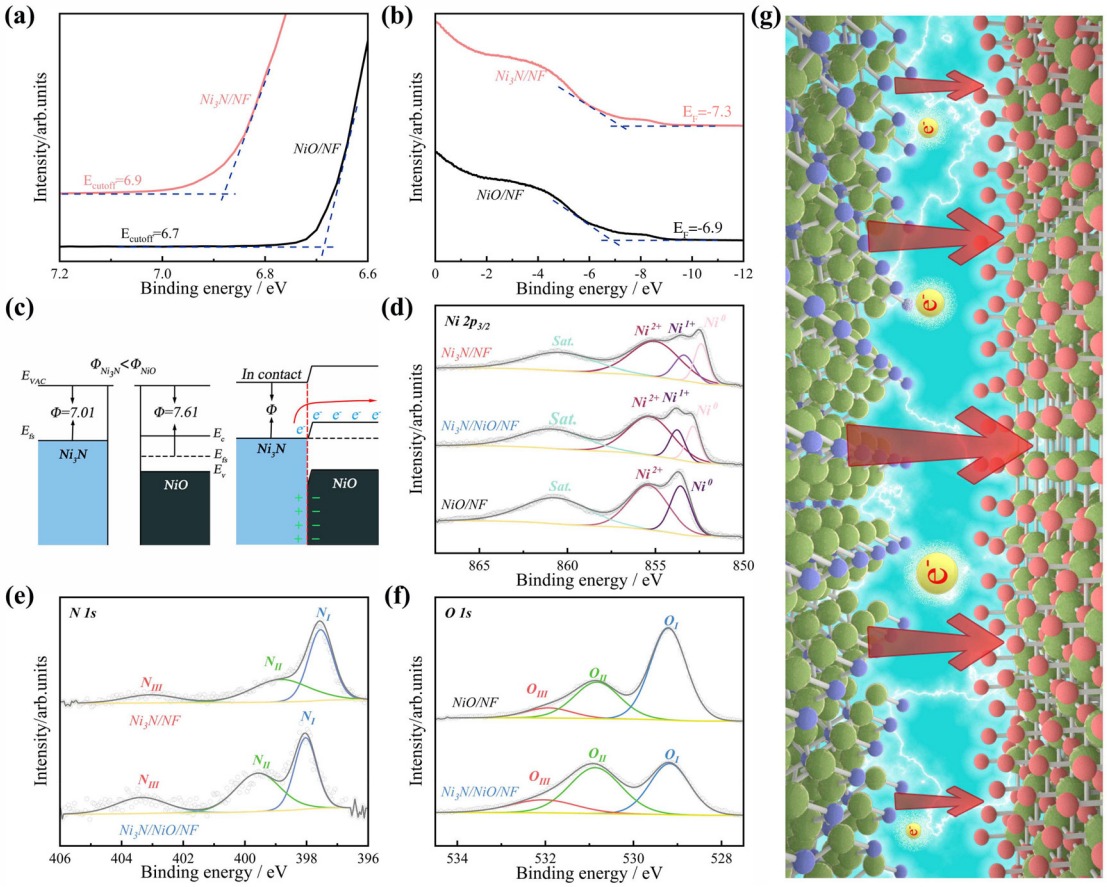

Fig. 3 UPS spectra of Ni_3N/NF and NiO/NF: (a) E_{cutoff} and (b) E_F representing the low-energy cutoff edge and Fermi energy level, respectively. (c) Energy band diagram of Ni_3N and NiO/NF Schottky heterostructures before and after contact. The deconvoluted high-resolution Ni 2p (d), O 1s (e) and N 1s (f) XPS spectra of NiO/NF, Ni_3N/NF and Ni_3N/NiO/NF. (g) Schematic diagram of the charge transfer between Ni_3N and NiO.

and O in adsorbed H_2O and O_2 (O_{III}).[57,58] Similar to the trend of Ni^{2+}, O–M (529.20 eV) in the Ni_3N/NiO/NF sample also shifted toward lower binding energy by 0.13 eV. These results indicate that in binary components, as the electron density of Ni_3N decreased, its oxidation state increased, while as the electron density of NiO increased, its oxidation state decreased. Based on the UPS analysis results, Ni_3N and NiO formed a Schottky heterostructure, confirming the possibility of spontaneous electron transfer between the Ni_3N phase and the NiO phase in the binary heterogeneous catalyst structure, where the Ni_3N phase acted as an electron donor and the NiO phase as an electron acceptor (Fig. 3g).

Based on the hypotheses of this study, the theoretical process is speculated as follows: in the Ni_3N/NiO heterostructure, due to the significant difference in work functions between the two phases, a Schottky barrier is formed, leading to directional electron transfer at the interface. This electron redistribution phenomenon increases the electron density on the NiO side, exhibiting stronger hydrogen adsorption capability, while the Ni_3N side shows electrophilicity, which is favorable for hydrogen desorption reactions. In alkaline electrolyte environments, water molecules first dissociate on the NiO surface, forming OH^- and H_{ad}, corresponding to the Volmer step. Subsequently, the H_{ad} accumulated on the NiO surface undergoes spillover under the influence of interfacial charge, migrating from the NiO surface to the Ni_3N surface. During this process, H_{ad} is adsorbed by Ni_3N to form intermediates due to electrostatic interactions. Meanwhile, the surface structure and electronic environment of Ni_3N are more conducive to the Heyrovsky or Tafel steps, in which two H_{ad} species either combine or react with electrons and water molecules in solution, ultimately generating hydrogen gas, which is released.

The electrochemical stability of these prepared catalysts was evaluated using chronopotentiometry (CP) at a constant current density (10 mA cm^{-2}). As shown in Fig. 4a, Ni_3N/NiO/NF exhibited minimal potential decay during 10 hours of continuous operation. Furthermore, repeated linear sweep voltammetry (LSV) tests also confirmed that the catalyst showed a decay of only 7 mV at 100 mA cm^{-2} after 10 hours of CP testing (Fig. 4b). This may be attributed to the excellent wettability characteristics of the Ni_3N/NiO/NF electrode surface. The contact angle test results showed that after structural and compositional modifications, the electrode surface gradually

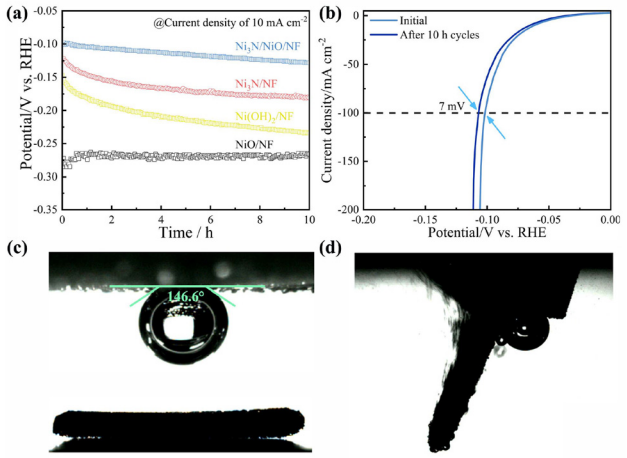

Fig. 4 (a) 10 h long-term chronopotentiometry of NiO/NF, $Ni(OH)_2$/NF, Ni_3N/NF and Ni_3N/NiO/NF at 10 mA cm^{-2}; (b) LSV curves of Ni_3N/NiO/NF before and after 10 hours of cycling; (c) contact angle test of Ni_3N/NiO/NF and (d) an image of the hydrogen evolution process at a current density of 50 mA cm^{-2}.

developed superhydrophilic and superaerophobic characteristics (Fig. S18 and 19 and Fig. 4c and d). These surface properties help facilitate rapid diffusion and adsorption of water molecules, enabling efficient detachment of hydrogen bubbles, thereby avoiding the shielding of active sites by bubbles and improving the reaction efficiency. Meanwhile, the hydrogen evolution video of the electrode shown in the figure indicates that compared to electrodes such as NF, bubbles on the Ni_3N/NiO/NF electrode surface can detach at high frequency with small sizes, minimizing mechanical structural damage. The XRD and SEM images shown in Fig. S20 further demonstrate that in addition to maintaining catalytic activity, the Ni_3N/NiO/NF electrode also exhibits good stability in terms of mechanical structure and compositional components.

Conclusions

A 3D Ni_3N/NiO/NF heterostructured electrode was developed in this study and its synergistic catalytic mechanism was investigated for the alkaline HER. The Ni_3N/NiO heterostructure leverages the catalytic advantages of NiO in water dissociation and Ni_3N in hydrogen adsorption and desorption, with the hydrogen spillover effect playing a critical role at the heterointerface. Electrochemical tests demonstrated the excellent catalytic activity and stability of Ni_3N/NiO/NF, requiring only 58 and 98 mV overpotentials to achieve current densities of 10 and 100 mA cm^{-2}, respectively, with a low Tafel slope of 42 mV dec^{-1}. Additionally, the superhydrophilic–superaerophobic interface significantly improved reactant diffusion and product desorption, ensuring long-term stability under operating conditions. This work highlights the potential of Ni_3N/NiO heterostructures as efficient and stable HER catalysts and provides valuable insights into the design of advanced materials for industrial-scale water electrolysis.

Conflicts of interest

The authors declare that they have no conflicts of interest.

Data availability

The data supporting this article have been included as part of the supplementary information (SI). Supplementary information: additional SEM images, XRD patterns, TEM images, elemental mappings, EIS fitting parameters, contact angle measurements, CV curves, and further experimental details. See DOI: https://doi.org/10.1039/d6dt00031b.

Acknowledgements

The authors thank the Natural Science Foundation of Shandong Province of China for research grant number ZR2022MB118.

References

1 H. Yang, M. Driess and P. W. Menezes, *Adv. Energy Mater.*, 2021, **11**, 2102074.
2 Y. Zeng, M. Zhao, Z. Huang, W. Zhu, J. Zheng, Q. Jiang, Z. Wang and H. Liang, *Adv. Energy Mater.*, 2022, **12**, 2201713.
3 B. Liu, Y. Li, P. Ding, D. Li, J. Li, X. Zhao, J. Zu, M. Wang, Y. Sun and M. Yu, *Appl. Catal., B*, 2026, **387**, 126514.
4 Y. Zhou, Z. Wang, M. Cui, H. Wu, Y. Liu, Q. Ou, X. Tian and S. Zhang, *Adv. Funct. Mater.*, 2024, **34**, 2410618.
5 I. Katsounaros, S. Cherevko, A. R. Zeradjanin and K. J. J. Mayrhofer, *Angew. Chem., Int. Ed.*, 2014, **53**, 102–121.
6 M. N. Hossain, L. Zhang, R. Neagu and E. Rassachack, *Electrochem. Energy Rev.*, 2024, **7**, 5.
7 Z. Geng, Z. Feng, H. Kong, J. Su, K. Zhang, J. Li, X. Sun, X. Liu, L. Ge, P. Gai and F. Li, *Adv. Sci.*, 2024, **11**, 2406843.
8 Y. Xu, C. Wang, Y. Huang and J. Fu, *Nano Energy*, 2021, **80**, 105545.
9 K. Veeramani, G. Janani, J. Kim, S. Surendran, J. Lim, S. C. Jesudass, S. Mahadik, H. Lee, T.-H. Kim, J. K. Kim and U. Sim, *Renewable Sustainable Energy Rev.*, 2023, **177**, 113227.
10 M. Jin, X. Zhang, S. Niu, Q. Wang, R. Huang, R. Ling, J. Huang, R. Shi, A. Amini and C. Cheng, *ACS Nano*, 2022, **16**, 11577–11597.
11 H. Shi, T.-Y. Dai, X.-Y. Sun, Z.-L. Zhou, S.-P. Zeng, T.-H. Wang, G.-F. Han, Z. Wen, Q.-R. Fang, X.-Y. Lang and Q. Jiang, *Adv. Mater.*, 2024, **36**, 2406711.
12 Z.-H. Yuan, T.-J. Wang, B. Sun, Q.-L. Hong, X. Ai, S.-N. Li, J. Bai and Y. Chen, *Appl. Catal., B*, 2025, **366**, 125041.

13 B. Sun, W. Zhong, H. Liu, X. Ai, S. Han and Y. Chen, *EnergyChem*, 2025, **7**, 100148.
14 Q. Xiang, J. Wang, Q. Miao, P. Tao, C. Song, W. Shang, T. Deng, Z. Yin and J. Wu, *Mater. Today Nano*, 2021, **15**, 100120.
15 Y. Zhao, Q. Sun, C. Zhang, F. Liu, L. Wang and G.-R. Xu, *J. Alloys Compd.*, 2023, **968**, 172286.
16 Y. Dong, H. Wang, X. Wang, H. Wang, Q. Dong, W. Wang, X. Wei, J. Ren, J. Liu and R. Wang, *Chem. Eng. J.*, 2024, **488**, 150953.
17 Q.-L. Hong, X. Xiao, X. Ai, H. Liu, G.-R. Xu, Q. Xue, X. Wang, B. Y. Xia and Y. Chen, *Chem. Soc. Rev.*, 2025, **54**, 9849–9875.
18 Z. W. Seh, J. Kibsgaard, C. F. Dickens, I. Chorkendorff, J. K. Nørskov and T. F. Jaramillo, *Science*, 2017, **355**, eaad4998.
19 Y. Zheng, Y. Jiao, A. Vasileff and S.-Z. Qiao, *Angew. Chem., Int. Ed.*, 2018, **57**, 7568–7579.
20 W. Zhang, Y. Zou, H. Liu, S. Chen, X. Wang, H. Zhang, X. She and D. Yang, *Nano Energy*, 2019, **56**, 813–822.
21 Y.-N. Zhou, W.-H. Hu, Y.-N. Zhen, B. Dong, Y.-W. Dong, R.-Y. Fan, B. Liu, D.-P. Liu and Y.-M. Chai, *Appl. Catal., B*, 2022, **309**, 121230.
22 J. R. Kitchin, J. K. Nørskov, M. A. Barteau and J. G. Chen, *J. Chem. Phys.*, 2004, **120**, 10240–10246.
23 P. Zhai, Y. Zhang, Y. Wu, J. Gao, B. Zhang, S. Cao, Y. Zhang, Z. Li, L. Sun and J. Hou, *Nat. Commun.*, 2020, **11**, 5462.
24 F. Yu, H. Zhou, Y. Huang, J. Sun, F. Qin, J. Bao, W. A. Goddard, S. Chen and Z. Ren, *Nat. Commun.*, 2018, **9**, 2551.
25 L. Zhao, Y. Zhang, Z. Zhao, Q.-H. Zhang, L.-B. Huang, L. Gu, G. Lu, J.-S. Hu and L.-J. Wan, *Natl. Sci. Rev.*, 2019, **7**, 27–36.
26 H. Li, M. Abdelgaid, J. R. Paudel, N. P. Holzapfel, V. Augustyn, J. R. McKone, G. Mpourmpakis and E. J. Crumlin, *J. Am. Chem. Soc.*, 2025, **147**, 6472–6479.
27 Y. Jin, X. Sun, H. Zhong, Z. Cheng, G. Lan, S. Wei, M. Sun, H. Liu and Y. Li, *Appl. Catal., B*, 2026, **382**, 125980.
28 J. Li, J. Hu, M. Zhang, W. Gou, S. Zhang, Z. Chen, Y. Qu and Y. Ma, *Nat. Commun.*, 2021, **12**, 3502.
29 K. Oldham and J. Myland, *Fundamentals of electrochemical science*, Elsevier, 2012.
30 C. Zhang, Z. Xu, N. Han, Y. Tian, T. Kallio, C. Yu and L. Jiang, *Sci. Adv.*, 2023, **9**, eadd6978.
31 Y. Sun, C. Zhang, Z. Guo, K. Liu, L. Jiang and C. Yu, *Adv. Funct. Mater.*, 2025, **35**, 2425150.
32 H. Wang, X. Xue, M. Fan, Y. Dong, H. Wang, X. Wang, Q. Dong, W. Wang, R. Wang and J. Liu, *Nano Lett.*, 2026, **26**, 1059–1067.
33 Z. Li, H. Wang, S. Ji, M. Fan, R. Jiang, J. Liu, X. Wang, H. Wang and R. Wang, *Chem. Eng. Sci.*, 2026, **320**, 122472.
34 Z. Lu, Y. Li, X. Lei, J. Liu and X. Sun, *Mater. Horiz.*, 2015, **2**, 294–298.
35 P. A. Kempler, R. H. Coridan and N. S. Lewis, *Energy Environ. Sci.*, 2020, **13**, 1808–1817.
36 C. Yu, P. Zhang, J. Wang and L. Jiang, *Adv. Mater.*, 2017, **29**, 1703053.
37 Y. Dong, X. Zhang, X. Wang, F. Liu, J. Ren, H. Wang and R. Wang, *J. Colloid Interface Sci.*, 2023, **636**, 657–667.
38 Y. Dong, S. Ji, H. Wang, V. Linkov and R. Wang, *Dalton Trans.*, 2022, **51**, 9681–9688.
39 R. L. Doyle and M. E. G. Lyons, *Phys. Chem. Chem. Phys.*, 2013, **15**, 5224–5237.
40 Y. Li, Y. Wu, M. Yuan, H. Hao, Z. Lv, L. Xu and B. Wei, *Appl. Catal., B*, 2022, **318**, 121825.
41 J. Shin, Y. J. Lee, A. Jan, S. M. Choi, M. Y. Park, S. Choi, J. Y. Hwang, S. Hong, S. G. Park, H. J. Chang, M. K. Cho, J. P. Singh, K. H. Chae, S. Yang, H.-I. Ji, H. Kim, J.-W. Son, J.-H. Lee, B.-K. Kim, H.-W. Lee, J. Hong, Y. J. Lee and K. J. Yoon, *Energy Environ. Sci.*, 2020, **13**, 4903–4920.
42 G. B. Kauffman, *Angew. Chem., Int. Ed.*, 2009, **48**, 1532–1533.
43 A. Alobaid, C. Wang and R. A. Adomaitis, *J. Electrochem. Soc.*, 2018, **165**, J3395.
44 J. Li, H.-X. Liu, W. Gou, M. Zhang, Z. Xia, S. Zhang, C.-R. Chang, Y. Ma and Y. Qu, *Energy Environ. Sci.*, 2019, **12**, 2298–2304.
45 A. Damian and S. Omanovic, *J. Power Sources*, 2006, **158**, 464–476.
46 M. M. Jaksic, J. Brun, B. Johansen and R. Tunold, *Int. J. Hydrogen Energy*, 1995, **20**, 265–273.
47 P. Krawczyk, T. Rozmanowski and M. Osińska, *Int. J. Hydrogen Energy*, 2016, **41**, 20433–20438.
48 Z. Li, Z. Gao, B. Li, L. Zhang, R. Fu, Y. Li, X. Mu and L. Li, *Appl. Catal., B*, 2020, **262**, 118276.
49 Y. Dong, Y. Wu, X. Wang, H. Wang, J. Ren, P. Wang, L. Pan, G. Wang and R. Wang, *Nanoscale*, 2023, **15**, 1813–1823.
50 C. Wang, H. Lu, Z. Mao, C. Yan, G. Shen and X. Wang, *Adv. Funct. Mater.*, 2020, **30**, 2000556.
51 C. Li, Y. Liu, Z. Zhuo, H. Ju, D. Li, Y. Guo, X. Wu, H. Li and T. Zhai, *Adv. Energy Mater.*, 2018, **8**, 1801775.
52 D. Zhang, H. Li, A. Riaz, A. Sharma, W. Liang, Y. Wang, H. Chen, K. Vora, D. Yan, Z. Su, A. Tricoli, C. Zhao, F. J. Beck, K. Reuter, K. Catchpole and S. Karuturi, *Energy Environ. Sci.*, 2022, **15**, 185–195.
53 T. Liu, M. Li, C. Jiao, M. Hassan, X. Bo, M. Zhou and H.-L. Wang, *J. Mater. Chem. A*, 2017, **5**, 9377–9390.
54 L. Liu, F. Yan, K. Li, C. Zhu, Y. Xie, X. Zhang and Y. Chen, *J. Mater. Chem. A*, 2019, **7**, 1083–1091.
55 L. Yu, Q. Zhu, S. Song, B. McElhenny, D. Wang, C. Wu, Z. Qin, J. Bao, Y. Yu, S. Chen and Z. Ren, *Nat. Commun.*, 2019, **10**, 5106.
56 C. Zhu, A.-L. Wang, W. Xiao, D. Chao, X. Zhang, N. H. Tiep, S. Chen, J. Kang, X. Wang, J. Ding, J. Wang, H. Zhang and H. J. Fan, *Adv. Mater.*, 2018, **30**, 1705516.
57 M. Chen, D. Liu, B. Zi, Y. Chen, D. Liu, X. Du, F. Li, P. Zhou, Y. Ke, J. Li, K. H. Lo, C. T. Kwok, W. F. Ip, S. Chen, S. Wang, Q. Liu and H. Pan, *J. Energy Chem.*, 2022, **65**, 405–414.
58 K. Hu, M. Wu, S. Hinokuma, T. Ohto, M. Wakisaka, J.-i. Fujita and Y. Ito, *J. Mater. Chem. A*, 2019, **7**, 2156–2164.

